Measurement of the antineutrino to neutrino charged-current interaction cross section ratio in MINERvA

L. Ren,[1] L. Aliaga,[2,3,§] O. Altinok,[4] L. Bellantoni,[5] A. Bercellie,[6] M. Betancourt,[5] A. Bodek,[6] A. Bravar,[7] H. Budd,[6] T. Cai,[6] M. F. Carneiro,[8] H. da Motta,[9] J. Devan,[2] S. A. Dytman,[1] G. A. Díaz,[6,3] B. Eberly,[1,*] E. Endress,[3] J. Felix,[10] L. Fields,[5,11] R. Fine,[6] A. M. Gago,[3] R. Galindo,[12] H. Gallagher,[4] A. Ghosh,[12,9] T. Golan,[6,5] R. Gran,[13] J. Y. Han,[1] D. A. Harris,[5] K. Hurtado,[9,14] M. Kiveni,[5] J. Kleykamp,[6] M. Kordosky,[2] T. Le,[4,15] E. Maher,[16] S. Manly,[6] W. A. Mann,[4] C. M. Marshall,[6,†] D. A. Martinez Caicedo,[9,‡] K. S. McFarland,[6,5] C. L. McGivern,[1,§] A. M. McGowan,[6] B. Messerly,[1] J. Miller,[12] A. Mislivec,[6] J. G. Morfín,[5] J. Mousseau,[17,‖] D. Naples,[1] J. K. Nelson,[2] A. Norrick,[2] Nuruzzaman,[15,12] V. Paolone,[1] J. Park,[6] C. E. Patrick,[11] G. N. Perdue,[5,6] M. A. Ramírez,[10] R. D. Ransome,[15] H. Ray,[17] D. Rimal,[17] P. A. Rodrigues,[18,6] D. Ruterbories,[6] H. Schellman,[8,11] C. J. Solano Salinas,[14] M. Sultana,[6] S. Sánchez Falero,[3] E. Valencia,[2,10] T. Walton,[19,§] J. Wolcott,[6,¶] M. Wospakrik,[17] and B. Yaeggy[12]

(MINERvA Collaboration)

[1]Department of Physics and Astronomy, University of Pittsburgh, Pittsburgh, Pennsylvania 15260, USA
[2]Department of Physics, College of William and Mary, Williamsburg, Virginia 23187, USA
[3]Sección Física, Departamento de Ciencias, Pontificia Universidad Católica del Perú, Apartado 1761, Lima, Peru
[4]Physics Department, Tufts University, Medford, Massachusetts 02155, USA
[5]Fermi National Accelerator Laboratory, Batavia, Illinois 60510, USA
[6]University of Rochester, Rochester, New York 14627 USA
[7]University of Geneva, 1211 Geneva 4, Switzerland
[8]Department of Physics, Oregon State University, Corvallis, Oregon 97331, USA
[9]Centro Brasileiro de Pesquisas Físicas, Rua Dr. Xavier Sigaud 150, Urca, Rio de Janeiro, Rio de Janeiro 22290-180, Brazil
[10]Campus León y Campus Guanajuato, Universidad de Guanajuato, Lascurain de Retana No. 5, Colonia Centro, Guanajuato 36000, Guanajuato México
[11]Northwestern University, Evanston, Illinois 60208
[12]Departamento de Física, Universidad Técnica Federico Santa María, Avenida España 1680 Casilla 110-V, Valparaíso, Chile
[13]Department of Physics, University of Minnesota—Duluth, Duluth, Minnesota 55812, USA
[14]Universidad Nacional de Ingeniería, Apartado 31139, Lima, Peru
[15]Rutgers, The State University of New Jersey, Piscataway, New Jersey 08854, USA
[16]Massachusetts College of Liberal Arts, 375 Church Street, North Adams, Massachusetts 01247, USA
[17]University of Florida, Department of Physics, Gainesville, Florida 32611, USA
[18]University of Mississippi, Oxford, Mississippi 38677, USA
[19]Hampton University, Department of Physics, Hampton, Virginia 23668, USA

We present measurements of the neutrino and antineutrino total charged-current cross sections on carbon and their ratio using the MINERvA scintillator-tracker. The measurements span the energy range 2–22 GeV and were performed using forward and reversed horn focusing modes of the Fermilab low-energy NuMI beam to obtain large neutrino and antineutrino samples. The flux is obtained using a subsample of charged-current events at low hadronic energy transfer along with precise higher energy external neutrino cross section data overlapping with our energy range between 12–22 GeV. We also report on the antineutrino-neutrino cross section ratio, R_{CC}, which does not rely on external normalization information. Our ratio measurement, obtained within the same experiment using the same technique, benefits from the cancellation of common sample systematic uncertainties and reaches a precision of ~5% at low energy. Our results for the antineutrino-nucleus scattering cross section and for R_{CC} are the most precise to date in the energy range $E_\nu < 6$ GeV.

---

[*]Present address: SLAC National Accelerator Laboratory, Stanford, CA 94309, USA.
[†]Present address: Lawrence Berkeley National Laboratory, Berkeley, CA 94720, USA.
[‡]Present address: Illinois Institute of Technology, Chicago, IL 60616, USA.
[§]Present address: Fermi National Accelerator Laboratory, Batavia, IL 60510, USA.
[‖]Present address: University of Michigan, Ann Arbor, MI 48109, USA.
[¶]Present address: Tufts University, Medford, MA 02155, USA.

I. INTRODUCTION

Long-baseline oscillation experiments [1,2], which aim to precisely measure neutrino oscillation parameters and constrain CP violation, will make use of neutrino and antineutrino beams in the few-GeV neutrino energy (E_ν) range. For appropriate baselines and energies, neutrino oscillation phenomena produce distinct shape signatures on either $\nu_\mu \to \nu_e$ or $\bar{\nu}_\mu \to \bar{\nu}_e$ appearance probabilities, which, in matter, depend on the CP violating phase (δ_{CP}) and the (unknown) sign of the mass splitting term, Δm^2_{31}. Variations of oscillation parameters over their allowed ranges produce degenerate effects on the appearance probabilities, complicating these measurements. Uncertainties in poorly constrained cross section components in this energy range produce further competing shape effects on the measured visible energy spectra used to extract the oscillation probabilities. Utilizing beams of both neutrinos and antineutrinos allows a measurement of the CP asymmetry [3], $\mathcal{A}_{CP}$, defined as,

$$\mathcal{A}_{CP} = \frac{P(\nu_\mu \to \nu_e) - P(\bar{\nu}_\mu \to \bar{\nu}_e)}{P(\nu_\mu \to \nu_e) + P(\bar{\nu}_\mu \to \bar{\nu}_e)}, \qquad (1)$$

which can be written in terms of probability ratios. Reducing uncertainties on the cross sections, and in particular their ratio, $R_{CC} = \sigma^{\bar{\nu}}/\sigma^\nu$, to which $\mathcal{A}_{CP}$ is primarily sensitive, is essential to achieving ultimate sensitivity in oscillation measurements.

The results presented here use neutrino and antineutrino events analyzed in the MINERvA scintillator (CH) detector exposed to the NuMI (Neutrinos at the Main Injector) beam. Total cross sections are extracted from selected charged-current (CC) event samples, and incident fluxes are measured *in situ* using a subsample of these events at low-ν (ν is the energy transferred to the hadronic system) as in our previous result [4]. The ratio, R_{CC}, is obtained by forming ratios of measured event rates in the two beam modes. Since the measurements are performed using the same apparatus and flux measurement technique, common detector and model related systematic uncertainties cancel in the ratio, resulting in a precise measurable quantity that can be leveraged to tune models and improve knowledge of interaction cross sections.

While knowledge of neutrino cross sections has recently been improved in the low-energy region, there is a dearth of precise antineutrino cross section measurements at low energies (below 10 GeV) [5]. The cross section ratio, R_{CC}, has recently been measured by MINOS [6] on iron with a precision of ~7% at 6 GeV. At lower energies, only one dedicated measurement [7] (on CF_3Br) has been performed, with a precision of ~20%. Measurements on a range of nuclear targets are needed to constrain nuclear dependence which currently contributes significantly to modeling uncertainty. While much of the existing data is on an iron nucleus, this result provides data on a light nuclear target (carbon). We improve on the precision of both the antineutrino cross section and R_{CC} (by nearly a factor of 4) at low energies (2–6 GeV).

Systematic uncertainties in our measured cross sections are dominated at the lowest energies by the limited knowledge of cross section model components at low hadronic energy transfer ($\lesssim 1$ GeV). The current suite of neutrino generators [8–14] are known to be deficient in modeling nuclear effects and detailed exclusive process rates at low energy transfer. To allow our measurement to be updated with future models, we also present the measured rates (corrected for detector effects and backgrounds) with the primary model-dependent terms factorized.

We have previously reported an inclusive CC cross section measurement [4] using the same data sample and method to constrain the flux shape with energy. The results presented here use an updated cross section model which has been tuned to improve agreement with our data in the low-ν region [15] as described in Sec. III. The current work also provides a precise measurement of the ratio, R_{CC}, as well as the measured model-independent rates for re-extracting cross sections with alternative generator-level models. In addition, the antineutrino flux normalization method employed here improves the antineutrino cross section precision by a factor of 1.5–1.9, which for the previous result was dominated by the large uncertainty (~10%) on the model-based antineutrino normalization constraint.

II. MINERVA EXPERIMENT

Muon neutrinos and antineutrinos are produced in NuMI when 120 GeV protons from the Fermilab Main Injector strike a graphite target. Details of the NuMI beam line can be found in Ref. [16]. A system of two magnetic horns is used to focus emerging secondary pions and kaons, which are allowed to decay in the 675 m space immediately downstream of the target. We analyze exposures in two low-energy NuMI beam modes. The forward horn current (FHC) mode sets the horn polarity to focus positively charged secondary beam particles, which results in a primarily muon neutrino beam (10.4% muon antineutrino component) with 3 GeV peak energy. If the polarity of both horns is reversed (RHC mode) the resulting beam has a large fraction of muon antineutrinos with the same peak beam energy and a sizable muon neutrino component (17.7%) that extends to high energies. Figure 1 shows the simulated fluxes [17] for muon neutrinos and antineutrinos in each mode. We use samples collected between March 2010 and April 2012 corresponding to exposures of 3.20×10^{20} protons on target (POT) in FHC and 1.03×10^{20} POT in RHC beam modes.

The MINERvA fine-grained scintillator tracking detector [18] is situated approximately 1 km downstream of the NuMI target. The active detector consists of triangular scintillator strips with height 1.7 cm and base 3.3 cm
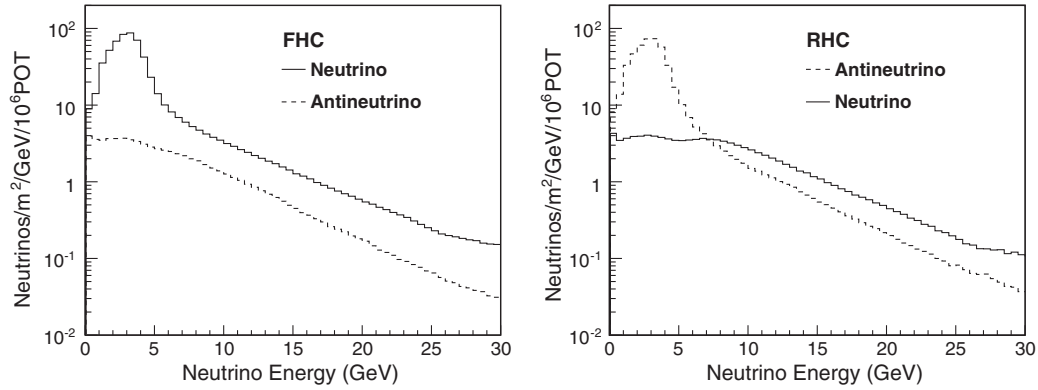
FIG. 1.   Predicted incident neutrino fluxes at the MINERvA detector in FHC (left) and RHC (right) beam modes from Ref. [17].

arranged into hexagonal X, U and V planes (at 60° with respect to one another) and giving single-plane position resolution of about 2.5 mm. We use events originating in the 6 ton fully active scintillator region that is primarily composed of carbon nuclei (88.5% carbon, 8.2% hydrogen, 2.5% oxygen and a number of other nuclei that make up the remaining fraction, by mass). We report results on a carbon target by correcting for the MINERvA target proton excess (see Sec. VI).

The downstream most plane of MINERvA is positioned 2 m upstream of the magnetized MINOS Near Detector [19] (MINOS ND), which is used to contain and momentum analyze muons exiting the MINERvA active detector volume. The detector geometry changes from sampling after every iron plane (2.54 cm thickness) to sampling every five iron-scintillator units after the first 7.2 m. This produces features in the measured muon momentum distribution and acceptance which will be discussed below. For the FHC (RHC) beam mode the MINOS ND toroidal magnetic field is set to focus negatively (positively) charged muons. Measurement of the direction of track curvature is used to tag the charge-sign of tracks, which is crucial to reducing the large wrong-sign beam background in the RHC mode.

III. MONTE CARLO SIMULATION

We use a custom MINERvA -tuned modification of GENIE 2.8.4 [20,21] referred to here as "GENIE-Hybrid" as input to simulated event samples as well as for the model correction terms needed to obtain our default cross section results. This model incorporates improved modeling of low-ν cross section components and is similar to that described in Ref. [15]. GENIE 2.8.4 uses a modified version of the relativistic Fermi gas model of the nucleus, which is inadequate to precisely describe neutrino scattering data at low three-momentum transfer such as quasielastic (QE) and $\Delta(1232)$ resonance production. For QE events, we use the random phase approximation (RPA) [22] model, which includes long-range nucleon-nucleon correlations to more

accurately characterize scattering from a nucleon bound in a nucleus. We also include the Valencia "2p2h" model contribution [23] of the neutrino interacting with a correlated nucleon pair that populates the energy transfer region between the QE and Δ-resonance events. Since even this does not adequately cover the observed signal excess in this region [15], we include additional modeling uncertainties from this contribution. In addition, we reduce the GENIE single pion nonresonant component[1] with initial state $\nu + n$ (or $\bar{\nu} + p$) by 57%, which has been shown to improve agreement with observed deuterium data [24].

IV. TECHNIQUE OVERVIEW

Events studied in this analysis are categorized as charged-current events by the presence of a long track originating from the primary interaction vertex which extrapolates into the MINOS ND. The inclusive sample, $N_{CC}^{\nu(\bar{\nu})}(E)$, is the number of measured charged current events in a neutrino energy bin E. We define $\mathcal{R}^{\nu(\bar{\nu})}(E)$, which is related to the fiducial cross section, as

$$\mathcal{R}^{\nu(\bar{\nu})}(E) = \frac{(N_{CC}^{\nu(\bar{\nu})}(E) - B_{CC}^{\nu(\bar{\nu})}(E)) \times A_{CC}^{\nu(\bar{\nu}),\mathrm{DET}}(E)}{(F^{\nu(\bar{\nu})}(E) - B_{\Phi}^{\nu(\bar{\nu})}(E)) \times A_{\Phi}^{\nu(\bar{\nu})}(E)}, \quad (2)$$

where superscript ν ($\bar{\nu}$) refers to neutrino (antineutrino). $F^{\nu(\bar{\nu})}(E)$ is the "flux sample" obtained from a subset of $N_{CC}^{\nu(\bar{\nu})}(E)$ with low hadronic energy (discussed below). The terms $B_{CC}^{\nu(\bar{\nu})}(E)$ and $B_{\Phi}^{\nu(\bar{\nu})}(E)$ are backgrounds due to neutral current and wrong-sign beam contamination in the inclusive and flux samples, respectively. Terms $A_{CC}^{\nu(\bar{\nu}),\mathrm{DET}}(E)$ and $A_{\Phi}^{\nu(\bar{\nu})}(E)$ correct the cross section and flux respective samples for detector resolution and bin-migration effects. The numerator of Eq. (2), $\Gamma_{CC}^{\nu(\bar{\nu})}(E)$,

---

[1]The corresponding GENIE parameter is $R_{bkg}^{\nu n CC1\pi}$ for neutrino and $R_{bkg}^{\bar{\nu} p CC1\pi}$ for antineutrino [21].

$$\Gamma_{\text{CC}}^{\nu(\bar{\nu})}(E) = (N_{\text{CC}}^{\nu(\bar{\nu})}(E) - B_{\text{CC}}^{\nu(\bar{\nu})}(E)) \times A_{\text{CC}}^{\nu(\bar{\nu}),\text{DET}}(E), \quad (3)$$

is the fiducial event rate and is tabulated below. To obtain the incident beam flux, we employ the "low-ν" method described previously [4,6,25,26]. In brief, the differential dependence of the cross section in terms of ν is expanded in ν/E as

$$\frac{d\sigma^{\nu,\bar{\nu}}}{d\nu} = A\left(1 + \frac{B^{\nu,\bar{\nu}}}{A}\frac{\nu}{E} - \frac{C^{\nu,\bar{\nu}}}{A}\frac{\nu^2}{2E^2}\right), \quad (4)$$

where E is the incident neutrino energy. The coefficients A, $B^{\nu,\bar{\nu}}$, and $C^{\nu,\bar{\nu}}$ depend on integrals over structure functions (or form factors, in the low energy limit).

$$A = \frac{G_F^2 M}{\pi}\int F_2(x)\,dx, \quad (5)$$

$$B^{\nu,\bar{\nu}} = -\frac{G_F^2 M}{\pi}\int (F_2(x) \mp xF_3(x))\,dx, \quad (6)$$

and

$$C^{\nu,\bar{\nu}} = B^{\nu,\bar{\nu}} - \frac{G_F^2 M}{\pi}\int F_2(x)\left(\frac{1 + \frac{2Mx}{\nu}}{1 + R_L} - \frac{Mx}{\nu} - 1\right)dx. \quad (7)$$

In the limit of $\nu/E \to 0$, the B and C terms vanish and both cross sections approach A [defined in Eq. (5)], which is the same for neutrino and antineutrino probes scattering off an isoscalar target (up to a small correction for quark mixing). We count events below a maximum ν value (ν_0) and apply a model-based correction

$$S^{\nu(\bar{\nu}),\nu_0}(E) = \frac{\sigma^{\nu(\bar{\nu})}(\nu_0, E)}{\sigma^{\nu(\bar{\nu})}(\nu_0, E \to \infty)}, \quad (8)$$

to account for ν/E and $(\nu/E)^2$ terms in Eq. (4). The numerator in Eq. (8) is the value of the integrated cross section below our chosen ν_0 cut at energy E, and the denominator is its value in the high energy limit. For antineutrinos, the structure functions in Eq. (6) add, resulting in a larger energy dependent correction term than for the neutrino case where they are subtracted and partially cancel. The flux is then proportional to the corrected low-ν rate

$$\Phi^{\nu(\bar{\nu})}(E) \propto \frac{(F^{\nu(\bar{\nu})}(E) - B_\Phi^{\nu(\bar{\nu})}(E)) \times A_\Phi^{\nu(\bar{\nu})}(E)}{S^{\nu(\bar{\nu})}(\nu_0, E)}. \quad (9)$$

We obtain a quantity that is proportional to the total CC cross section,

$$\sigma_{\text{CC}}^{\nu(\bar{\nu})}(E) \propto \mathcal{R}^{\nu(\bar{\nu})} \times S^{\nu(\bar{\nu})}(\nu_0, E) \times A_{CC}^{\nu(\bar{\nu}),\text{KIN}}(E), \quad (10)$$

by applying a correction, $A^{\nu(\bar{\nu}),\text{KIN}}$, for regions outside of our experimental acceptance. The term $A^{\nu(\bar{\nu}),\text{KIN}}$ (discussed in Sec. VA) is computed from a generator level

Monte Carlo model. The rates, $\mathcal{R}^\nu$ and $\mathcal{R}^{\bar{\nu}}$, in each beam mode are used to obtain the ratio

$$R_{\text{CC}}(E) = \frac{\sigma_{\text{CC}}^{\bar{\nu}}(E)}{\sigma_{\text{CC}}^{\nu}(E)} = \frac{\mathcal{R}^{\bar{\nu}}}{\mathcal{R}^\nu}\left(\frac{A_{\text{CC}}^{\bar{\nu},\text{KIN}}(E) \times S^{\bar{\nu}}(\nu_0, E) \times H^\nu(\nu_0)}{A_{\text{CC}}^{\nu,\text{KIN}}(E) \times S^\nu(\nu_0, E) \times H^{\bar{\nu}}(\nu_0)}\right). \quad (11)$$

The terms $H^\nu(\nu_0)$ and $H^{\bar{\nu}}(\nu_0)$, which supply the absolute flux normalization in the low-ν method for neutrinos and antineutrinos, respectively, are related in the Standard Model and nearly cancel in this ratio. The measurements are performed using the same detector and beam line, which reduces the effect of some experimental uncertainties. The ratio measured in this technique also benefits from cancellation of correlated model terms; this cancellation reduces the modeling component of the systematic uncertainty relative to that for either neutrino or antineutrino measured cross section.

V. EVENT RECONSTRUCTION AND SELECTION

Neutrino events are reconstructed using timing and spatial information of energy deposited in the MINERvA scintillator. Hits are grouped in time into "slices" and within a slice, spatially into "clusters" which are used along with pattern recognition to identify tracks. The CC-inclusive event sample, denoted $N_{\text{CC}}^{\nu(\bar{\nu})}(E)$, is selected by requiring a primary track matched into the MINOS ND. MINOS-matched track momentum, E_μ, is reconstructed using either range, for tracks that stop and deposit all of their energy in the MINOS ND, or the measured curvature of the trajectory, for tracks which exit the MINOS ND. Tracks measured from range in MINOS have a momentum resolution of order 5% while those measured from curvature typically have a resolution of order 10%. Clusters not associated with the MINOS-matched muon track form the recoil system and are calorimetrically summed to obtain the hadronic energy, ν. Neutrino energy is constructed from the sum $E_\nu = E_\mu + \nu$. An event vertex is assigned by tracking the muon upstream through the interaction region until no energy is seen in an upstream cone around the track. The vertex is required to be within the fiducial region of the scintillator.

Additional track requirements are applied to improve energy resolution and acceptance. The track fitting procedure in the MINOS spectrometer yields a measurement of the momentum with an associated fractional uncertainty, which is required to be less than 30%. The charge-sign is determined by measuring the track curvature and is required to be negative for tracks in FHC mode and positive for those in RHC mode. We also require the muon track candidate to have a minimum energy $E_\mu > 1.8$ GeV and a maximum angle $\theta_\mu < 0.35$ rad (20°) with respect to the beam direction in the lab frame. The portion of the track
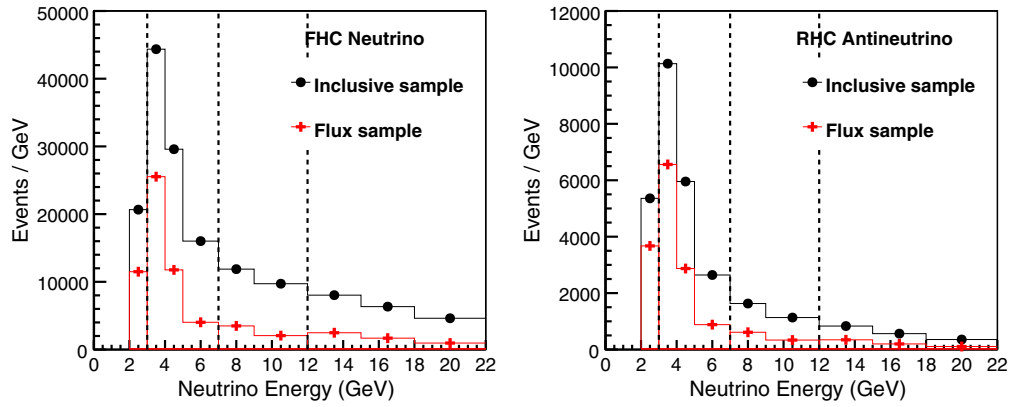
FIG. 2.   Neutrino inclusive ($N_{\mathrm{CC}}^{\nu(\bar{\nu})}$) and low-$\nu$ flux sample ($F^{\nu(\bar{\nu})}$) yields for FHC neutrino (left) and RHC antineutrino (right) modes. The dashed lines are plotted at the values where the flux sample ν_0 is changed. Statistical errors are too small to be visible on the points.

in MINOS is required to not pass through the uninstrumented coil hole region. Events in which the muon track ends less than 80 cm from the center of the coil hole are also removed. This removes 0.8% (0.4%) events from the neutrino (antineutrino) CC-inclusive sample.

The flux-extraction technique uses $F^{\nu(\bar{\nu})}(E)$, the number of CC-inclusive events in an energy bin below a maximum ν value. We choose this maximum value (ν_0) to vary with energy, keeping the energy dependent contributions in Eq. (4) small ($\lesssim 0.1$ for neutrinos and $\lesssim 0.2$ for antineutrinos) in the region where modeling uncertainties are sizable ($E_\nu < 7$ GeV), while at higher energies where we normalize to external data (12–22 GeV), it is increased to improve statistical precision. The values are $\nu_0 = 0.3$ GeV for $E_\nu < 3$ GeV, $\nu_0 = 0.5$ GeV for $3 < E_\nu < 7$ GeV, $\nu_0 = 1$ GeV for $7 < E_\nu < 12$ GeV and $\nu_0 = 2$ GeV for $E_\nu > 12$ GeV. The inclusive and flux sample overlap is less than 50% (60%) for neutrinos (antineutrinos).

A. Event rates

Figure 2 shows the measured inclusive and flux sample rates in the two beam modes. The fiducial event rate, $\Gamma_{\mathrm{CC}}^{\nu(\bar{\nu})}(E)$, [Eq. (3)] is determined by removing sample backgrounds and applying corrections for experimental acceptance. The components are described below and tabulated in Table I.

Backgrounds are dominated by the contribution from tracks with misidentified charge-sign which arise from the wrong-sign beam flux component (wrong-sign contamination). The background peaks at high energies in the RHC mode (about 4% above 10 GeV in the inclusive sample). The charge-sign and track quality requirements effectively reduce the wrong-sign contamination. The remaining background is estimated using the simulated wrong-sign beam flux shown in Fig. 1. The neutral current contribution is negligible ($\ll 1\%$) in both beam modes.

We correct for the experimental acceptance effects using a full detector simulation along with a tuned version of GENIE Monte Carlo (GENIE-Hybrid) which is described in Sec. III. We separate experimental acceptance terms into two contributions. The term $A_{\mathrm{CC}}^{\nu(\bar{\nu}),\mathrm{DET}}$, which represents the ratio of the number of events generated in a given neutrino energy bin to the number reconstructed in our event sample, accounts for detector resolution smearing and bin migration effects. Final state interaction (FSI) effects, which arise from reinteractions of emerging final state particles in the target nucleus, change the measured hadronic energy and also affect $A_{\mathrm{CC}}^{\nu(\bar{\nu}),\mathrm{DET}}$. This bin migration effect is included

TABLE I.   Neutrino and antineutrino inclusive, $N_{\mathrm{CC}}^{\nu(\bar{\nu})}$, and flux sample, $F^{\nu(\bar{\nu})}$, yields along with corresponding background contributions ($B_{\mathrm{CC}}^{\nu(\bar{\nu})}$ and $B_{\Phi}^{\nu(\bar{\nu})}$, respectively). The acceptance term, $A_{\mathrm{CC}}^{\nu(\bar{\nu}),\mathrm{DET}}$, is applied to obtain the fiducial event rate, $\Gamma_{\mathrm{CC}}^{\nu(\bar{\nu})}(E)$, from Eq. (3).

| ν_0 (GeV)	E (GeV)	N_{CC}^{ν}	B_{CC}^{ν}	$A_{\mathrm{CC}}^{\nu,\mathrm{DET}}$	F^{ν}	B_{Φ}^{ν}	A_{ϕ}^{ν}	$N_{\mathrm{CC}}^{\bar{\nu}}$	$B_{\mathrm{CC}}^{\bar{\nu}}$	$A_{\mathrm{CC}}^{\bar{\nu},\mathrm{DET}}$	$F^{\bar{\nu}}$	$B_{\Phi}^{\bar{\nu}}$	$A_{\phi}^{\bar{\nu}}$
0.3	2–3	20660	53	2.38	11493	29	1.94	5359	18	1.99	3673	6	1.60
	3–4	44360	61	2.30	25530	19	1.76	10133	25	1.94	6560	4	1.56
0.5	4–5	29586	65	1.92	11765	13	1.45	5955	24	1.65	2871	2	1.36
	5–7	32026	170	1.70	8046	29	1.34	5284	74	1.47	1764	4	1.27
1.0	7–9	23750	171	1.86	6980	32	1.59	3261	102	1.58	1224	6	1.50
	9–12	29161	207	1.95	6165	31	1.60	3400	141	1.66	1007	9	1.53
	12–15	24093	158	1.94	7438	39	1.42	2496	115	1.63	1033	9	1.42
2.0	15–18	19011	104	1.85	5041	17	1.28	1690	77	1.48	595	6	1.23
	18–22	18475	98	1.78	3826	14	1.25	1418	72	1.44	427	5	1.23
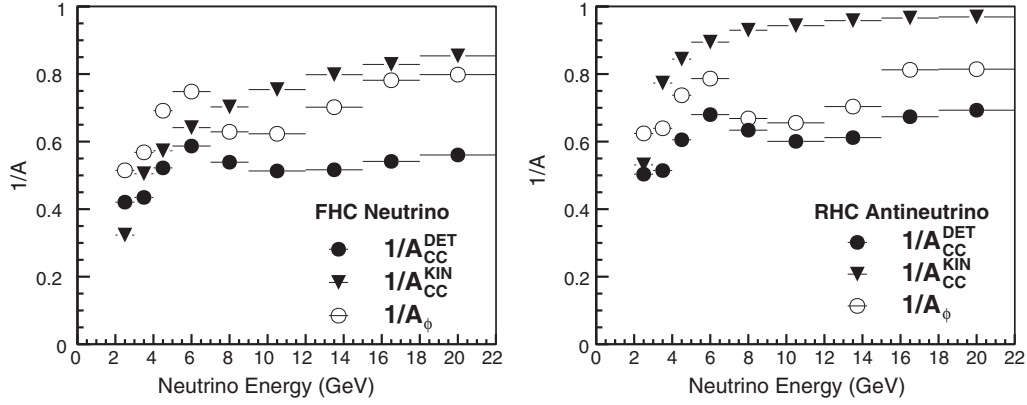
FIG. 3.   Reciprocal of acceptance components ($1/A_{CC}^{DET}$, $1/A^{KIN}$) for cross section and ($1/A_\Phi$) for flux samples of FHC neutrinos (left) and RHC antineutrinos (right).

in our Monte Carlo simulation model. The term $A_\Phi^{\nu(\bar\nu)}(E)$ is defined similarly with an additional maximum ν requirement. The fiducial event rate depends only on $A_{CC}^{\nu(\bar\nu),DET}$ and $A_\Phi^{\nu(\bar\nu)}(E)$ and is nearly generator model independent. The kinematic acceptance, A_{CC}^{KIN}, defined as the ratio of all generated events in a given bin to those with muon energy $E_\mu > 1.8$ GeV and angle $\theta_\mu < 0.35$ rad, must be applied to obtain a total cross section from the fiducial event rate. This term is computed directly from a generator level model. It is tabulated for our default model along with other model-dependent corrections in Table III. Nearly all muons in the selected flux sample automatically pass the kinematic cuts (except for a small fraction in the first energy bin which is computed to be 5.1% using the GENIE-Hybrid model and 4.9% using NuWro [14]). We therefore only report one acceptance, A_Φ, which includes the kinematic contribution in the flux sample.

Figure 3 shows the size of the acceptance correction terms for each sample. Kinematic acceptance is most important at lowest energies (primarily below 3 GeV), which have the largest fraction of events below muon energy threshold. The kinematic thresholds result in poorer overall acceptance at all energies for neutrinos compared with antineutrinos. This

is a consequence of the different inelasticity ($y = \nu/E_\nu$) dependence of the two cross sections, which produce a harder muon energy distribution for antineutrinos with correspondingly more forward-going muons. The flux sample with the $\nu < \nu_0$ requirement also selects a harder muon spectrum and results in better corresponding acceptance relative to the inclusive sample in both modes. The detector acceptance is above 50% for neutrino energies greater than 5 GeV. The shapes of $1/A_{CC}^{DET}$ and $1/A_\Phi$ are affected by the MINOS ND sampling geometry as well as the two methods of measuring momentum (from range and from curvature), which have different resolution. The dip in the 6–10 GeV region results from the contained (range) momentum sample decreasing while the curvature sample, which has poorer resolution, is becoming dominant.

VI. LOW-ν FLUX EXTRACTION

We obtain the shape of the flux with energy from the corrected flux yield using Eq. (9). The low-ν correction term is computed from Eq. (8) using the GENIE-Hybrid model as shown in Fig. 4 (also in Table III).

The neutrino flux is normalized using external neutrino cross section data overlapping our sample in the normalization bin, E_N, (neutrino energies 12–22 GeV).
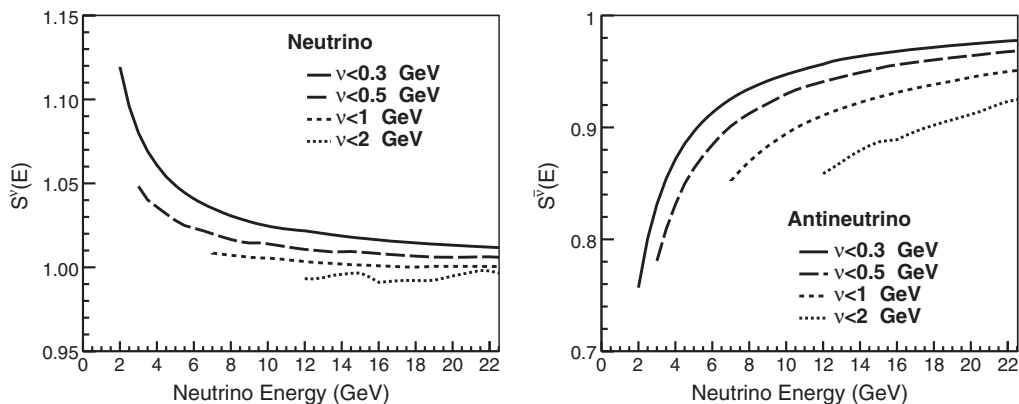

FIG. 4.   GENIE-hybrid based low-ν corrections, $S^{\nu(\bar\nu)}(\nu_0, E)$, for neutrinos (left) and antineutrinos (right).

TABLE II. Neutrino and antineutrino flux data and corrections needed to apply the normalization technique described in the text. The flux sample yield, $F^{\nu(\bar{\nu})}$, along with corresponding background contribution, $B_{\Phi}^{\nu(\bar{\nu})}$, and acceptance correction, $A_{\phi}^{\nu(\bar{\nu})}$, are ν_0 dependent and are used to compute the unnormalized cross section.

ν_0 (GeV)	E (GeV)	$F^\nu(E)$	$B_\Phi^\nu(E)$	$A_\phi^\nu(E)$	$H^\nu(\nu_0)$	$F^{\bar{\nu}}(E)$	$B_\Phi^{\bar{\nu}}(E)$	$A_\phi^{\bar{\nu}}(E)$	$\alpha(\nu_0)$
0.3	13.50	1315	10	1.18		247	1	1.04	
0.3	16.50	863	4	1.12	3.83 ± 0.091	147	1	0.94	1.126 ± 0.067
0.3	20.00	662	4	1.05		110	1	0.96	
0.5	13.50	2415	15	1.28		385	2	1.21	
0.5	16.50	1613	7	1.19	1.96 ± 0.035	224	1	1.09	1.056 ± 0.051
0.5	20.00	1190	4	1.16		159	2	1.12	
1.0	13.50	4419	25	1.36		636	5	1.33	
1.0	16.50	2967	12	1.25	1.02 ± 0.014	373	3	1.18	1.005 ± 0.039
1.0	20.00	2235	8	1.21		260	3	1.19	
2.0	13.50	7438	39	1.42		1033	9	1.42	
2.0	16.50	5041	17	1.28	0.574 ± 0.006	595	6	1.23	1
2.0	20.00	3826	14	1.25		427	5	1.23	

The NOMAD [27] measurement is singled out because it is the only independent result on the same nuclear target (carbon) in this range. The weighted average value of the NOMAD from 12–22 GeV is $\sigma_N^\nu/E_N = (0.699 \pm 0.025) \times 10^{-38}$ cm^2/GeV. We compute a weighted average value for our measured unnormalized neutrino cross section, $\sigma^{\nu,\nu_0}(E_N)$, from our points ($E = 13.5$, 16.5, and 20 GeV) in the normalization bin from Eq. (10). We obtain a normalization constant for each ν_0 subsample, $H^\nu(\nu_0)$, using

$$H^\nu(\nu_0) = \frac{\sigma^{\nu,\nu_0}(E_N) \times I_{\mathrm{iso}}^\nu(E_N)}{\sigma_N^\nu}, \qquad (12)$$

where the isoscalar correction, I_{iso}, accounts for the proton excess ($f_p = 54\%$, $f_n = 1 - f_p$) in the MINERvA target material obtained from

$$I_{\mathrm{iso}}^{\nu(\bar{\nu})}(E) = \left(\frac{\sigma_p^{\nu(\bar{\nu})}(E) + \sigma_n^{\nu(\bar{\nu})}(E)}{f_p \sigma_p^{\nu(\bar{\nu})}(E) + f_n \sigma_n^{\nu(\bar{\nu})}(E)} \right)$$
$$\times \left(\frac{f_p \sigma_p^{\nu(\bar{\nu})}(\nu_0, E) + f_n \sigma_n^{\nu(\bar{\nu})}(\nu_0, E)}{\sigma_p^{\nu(\bar{\nu})}(\nu_0, E) + \sigma_n^{\nu(\bar{\nu})}(\nu_0, E)} \right). \qquad (13)$$

Here, $\sigma_{p(n)}^{\nu(\bar{\nu})}(E)$ is the neutrino (antineutrino) cross section on a proton (neutron) in carbon and $\sigma_{p(n)}^{\nu(\bar{\nu})}(\nu_0, E)$ is its value for $\nu < \nu_0$. This correction, (see Table III), is negligible above 6 GeV and increases up to 4.2% in the lowest energy bin.

In the low-ν flux extraction method, neutrino and antineutrino cross sections in the low inelasticity limit $y \to 0$ are related, and approach the same constant value [Eq. (4)] for an isoscalar target in the absence of quark mixing. We make use of this to link the normalization of our low-ν antineutrino flux sample to that for neutrinos and therefore do not require external antineutrino cross section values. The weighted average (isoscalar corrected) unnormalized antineutrino cross section, $\sigma^{\bar{\nu},\nu_0}(E_N) \times I_{\mathrm{iso}}^{\bar{\nu}}(E_N)$, is computed in the normalization bin for each ν_0 value. It is linked to that for neutrinos by applying a small correction due to quark mixing, which is computed from a generator model

$$G(\nu_0) = \frac{\sigma^{\bar{\nu}}(\nu_0, E \to \infty)}{\sigma^\nu(\nu_0, E \to \infty)}. \qquad (14)$$

TABLE III. Neutrino and antineutrino cross section model dependent corrections computed using the GENIE-Hybrid model. $S^{\nu(\bar{\nu})}(\nu_0, E)$ is defined in Eq. (8), and $I_{\mathrm{iso}}^{\nu(\bar{\nu})}(\nu_0, E)$ is defined in Eq. (13).

E(GeV)	$A_{\mathrm{CC}}^{\nu,\mathrm{KIN}}(E)$	$S^\nu(\nu_0, E)$	$I_{\mathrm{iso}}^\nu(\nu_0, E)$	$A_{\mathrm{CC}}^{\bar{\nu},\mathrm{KIN}}(E)$	$S^{\bar{\nu}}(\nu_0, E)$	$I_{\mathrm{iso}}^{\bar{\nu}}(\nu_0, E)$
2.5	3.094	1.096	0.954	1.883	0.801	1.042
3.5	1.981	1.040	0.982	1.293	0.809	1.016
4.5	1.746	1.032	0.983	1.185	0.850	1.016
6	1.559	1.023	0.984	1.118	0.884	1.016
8	1.423	1.007	0.998	1.076	0.869	1.005
10.5	1.326	1.005	0.998	1.060	0.899	1.005
13.5	1.253	0.995	0.999	1.044	0.875	1.004
16.5	1.207	0.992	0.999	1.035	0.893	1.004
20	1.171	0.995	0.999	1.032	0.912	1.004

This correction, which is dominated by a term that is proportional to $V_{us}^2 \approx 0.05$, is negligible for $\nu_0 < 0.5$ GeV, 1.5% for $\nu_0 < 1$ GeV and 2.6% for $\nu_0 < 2$ GeV. We obtain a normalization factor for the $\nu_0 = 2$ GeV subsample from the corrected neutrino normalization, $H^{\bar{\nu}} = H^{\nu}/G$. Rather than treating each low-ν subsample independently, we take the $\nu_0 = 2$ GeV value as a standard and relatively normalize among different flux samples to make them match the same value in the normalization bin. We obtain the normalization for each ν_0 sample from $H^{\bar{\nu}}(\nu_0) = H^{\nu}(\nu_0)/G(\nu_0)/\alpha(\nu_0)$, where $\alpha(\nu_0)$ is the factor needed to adjust the measured antineutrino cross section at E_N to our measured value for $\nu_0 = 2$ GeV. This technique makes use of additional information in our low-ν data to compensate for unmodeled cross section contributions or energy dependent systematic uncertainties in that region. The values of α (given in Table II) range from 1.0 to 1.126. The size of the correction in the lowest energy bin is comparable to the size of the 1σ systematic error in the bin (9%). The additional statistical error from α is included in the result, and it dominates the statistical error in the antineutrino flux and R_{CC} below 7 GeV.

VII. SYSTEMATIC UNCERTAINTIES

We consider systematic uncertainties that arise from many sources including muon and hadron energy scales, reconstruction-related effects, cross section modeling, backgrounds, and normalization uncertainties. In each case, we evaluate the effect by propagating it through all the steps of the analysis, including a recalculation of the absolute normalization. The normalization technique makes the results insensitive to effects that change the overall rates.

The muon energy scale uncertainty is evaluated by adding the 2% range uncertainty [19] in quadrature with the uncertainty in momentum measured from curvature (2.5% for $P_\mu < 1$ GeV and 0.6% for $P_\mu > 1$ GeV), which is dominated by knowledge of the MINOS ND magnetic field [18]. A small component of energy loss uncertainty in MINERvA is also taken into account. The hadronic response uncertainty is studied by incorporating an individual response uncertainty for each final state particle produced at the hadronic vertex in the neutrino interaction. A small-scale functionally equivalent detector in a test beam [28] was used to assess energy responses and their uncertainties, which are found to be 3.5% for protons, and 5% for $\pi^{\pm}$ and K. In addition to the test beam study, information from an *in situ* Michel electron and π^0 samples is used to determine the 3% uncertainty in electromagnetic response. Low-energy neutrons have the largest uncertainties (25% for kinetic energies < 50 MeV and 10%–20% for > 50 MeV), which are estimated by benchmarking GEANT4 [29] neutron cross sections against $nA \rightarrow pX$ measurements in this energy range. The energy scale uncertainties are the most important components of the

flux shape measurement, but these largely cancel in cross sections and R_{CC}, resulting in a smaller overall effect.

Two reconstruction-related sources of uncertainty that affect measured shower energies were considered. The effect of PMT channel cross talk is studied by injecting cross talk noise into the simulation, and its uncertainty is estimated by varying the amount by 20%. The resulting uncertainty is small and is added in quadrature with the hadronic energy scale uncertainty. Muon track-related energy depositions (from δ rays or bremsstrahlung) are difficult to isolate within the shower region. We use data and simulation samples of beam-associated muons passing through the detector to model these and tune our hadron energy distribution in data and simulation. We compare two algorithms to separate muon-associated energy from the shower region and take their difference as the uncertainty from this source, which is also found to be small.

The effect of accidental activity from beam-associated muons is simulated by overlaying events from data within our reconstruction timing windows. We study overall reconstruction efficiency as a function of neutrino energy by projecting track segments reconstructed using only the MINERvA detector and searching for the track in MINOS ND, and vice versa. Track reconstruction efficiency, which agrees well between data and Monte Carlo simulations, is above 99.5% for MINERvA and above 96% for MINOS ND and is found to be nearly constant with energy. We adjust the simulated efficiency accordingly, although the normalization procedure makes the results insensitive to these effects.

Cross section model uncertainties enter into the measurement directly through the model-dependent correction as well as through bin migration effects at the boundaries of our experimental acceptance. Our default model (GENIE-Hybrid) is based on GENIE 2.8.4; we therefore use the prescription in Ref. [21] to evaluate uncertainties on all of the corresponding model parameters. The largest GENIE model uncertainties arise from final state interactions (FSI) and the resonance model parameters. We account for uncertainties in the resonance contribution by varying the axial mass parameters, M_A^{RES} and M_V^{RES}, in our model by $\pm 20\%$ and $\pm 10\%$, respectively. The resulting effect on the cross section is up to 4%. The GENIE parameters that control FSI effects include mean free path, reaction probabilities, nuclear size, formation time and hadronization model variation. The largest FSI uncertainty, due to the pion mean free path within the nucleus, is up to 2% (3%) for cross sections (fluxes). We separately evaluate the uncertainties from the tuned model components (RPA, single pion nonresonant, and 2p2h) discussed in Sec. III. We include half the difference between the default GENIE 2.8.4 and the implemented RPA model in quadrature into the total model uncertainty. We assume a 15% uncertainty in the retuned nonresonant single pion production component. After incorporating the 2p2h model, a sizable
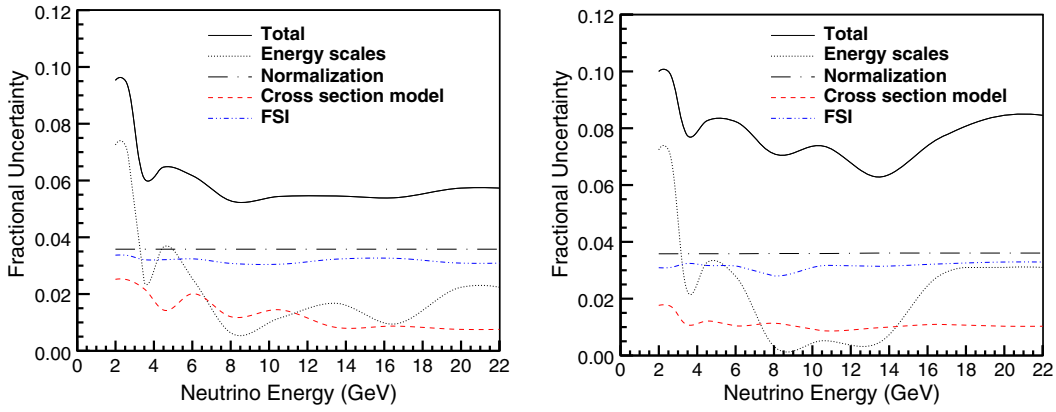
FIG. 5. Measurement uncertainties for neutrino (left) and antineutrino (right) low-ν fluxes. The total uncertainty (sys.+stat.) is the solid line. Components from the cross section model (dashed red), FSI (dot-dash blue), and energy scales (dotted) are shown. The 3.6% uncertainty in the external normalization (dashed black) is the error of the NOMAD data in the normalization region.
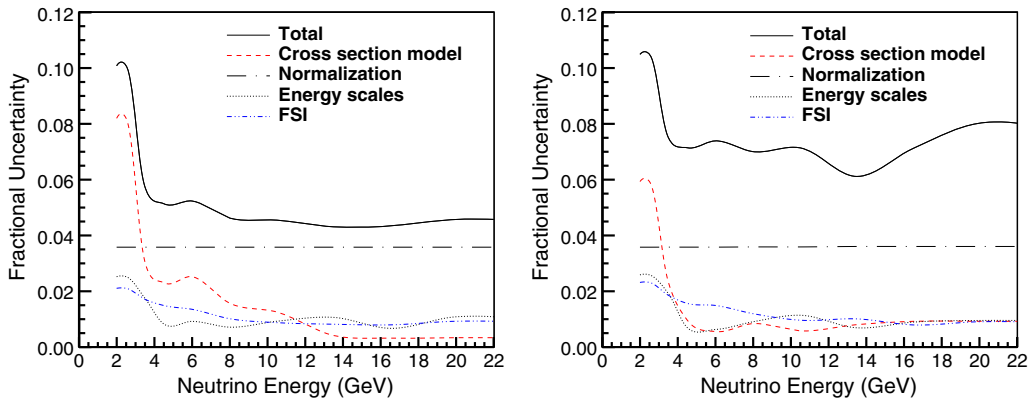

FIG. 6. Measurement uncertainties for neutrino (left) and antineutrino (right) total cross sections. The total uncertainty (sys.+stat.) is the solid line. Components from the cross section model (dashed red), FSI (dot-dash blue), and energy scales (dotted) are shown. The 3.6% uncertainty in the external normalization (dashed black) is the error of the NOMAD data in the normalization region. Statistical error dominates the measurement in the antineutrino result.

discrepancy in the hadronic energy distribution with the data remains. To assess an additional uncertainty from this unmodeled contribution, we fit the data excess at low hadronic energy described in Ref. [15] in the neutrino energy range $2 < E_\nu < 6$ GeV (taking into account separately proton-proton and proton-neutron initial states) to obtain a corrected model [30,31]. We take the uncertainty as the difference of the result obtained with this data-driven model, from the nominal result. The MINERvA antineutrino data also show an excess in the same region. We apply the corrected model from neutrino described above and then fit the remaining antineutrino excess to obtain a data-driven antineutrino 2p2h model uncertainty. The primary effect of varying the size of this contribution is to shift the overall level of the cross section. The normalization procedure removes most of the effect and the remaining uncertainty is less than 1.5% (2%) on the cross section (flux).

The contamination from wrong-sign events is significant only for the antineutrino sample (about 4% above 15 GeV).
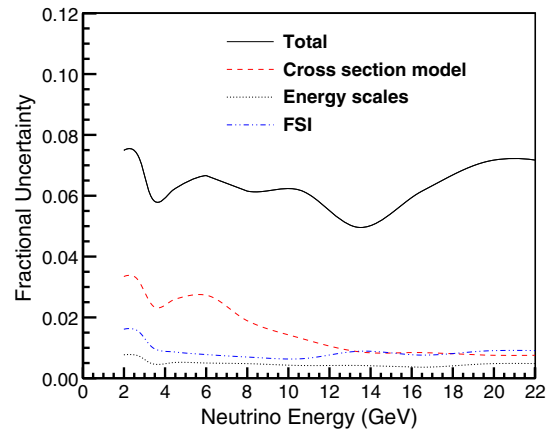

FIG. 7. Measurement uncertainties for the cross section ratio, R_{CC}. The total uncertainty (sys.+stat.) is the solid line. Components from the cross section model (dashed red), FSI (dot-dash blue), and energy scales (dotted) are shown. Normalization uncertainty is very small (<1%) and is included in the total error curve. The uncertainty is dominated by the statistical precision of the antineutrino sample.
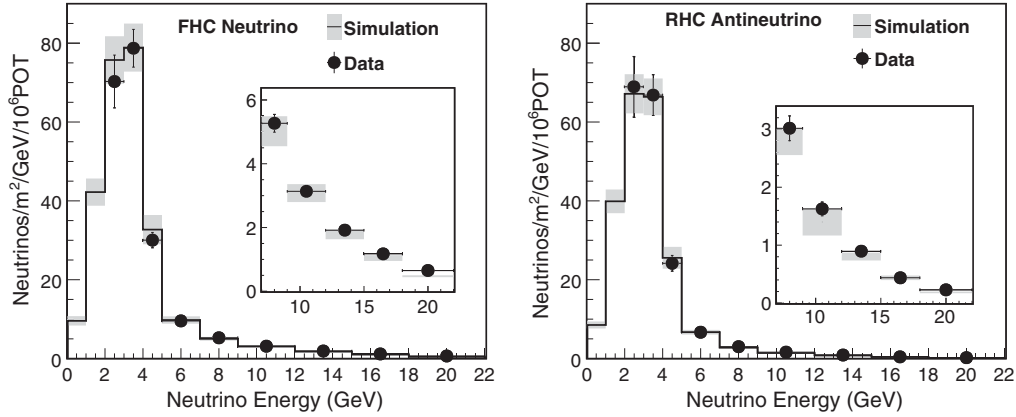
FIG. 8.   Extracted low-ν flux (points) for a FHC neutrino (left) and RHC antineutrino (right). The histogram shows the Monte Carlo simulated fluxes from Ref. [17] and one sigma error band (shaded bars). The insets show a zoom-in of the 7–22 GeV energy range.
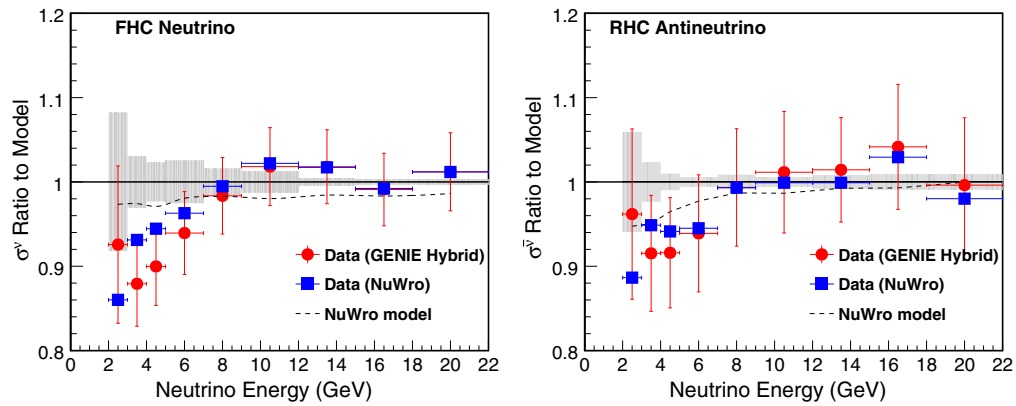

FIG. 9.   Ratio of the measured neutrino (left) and antineutrino (right) cross sections to the GENIE-Hybrid model. Points are MINERvA data with default GENIE-Hybrid (circles) and alternative NuWro model (squares) used to compute model-based correction terms. GENIE-Hybrid data points are plotted with total error (sys.+stat.). The dashed line shows the NuWro model. The shaded band give the size of the cross section model systematic uncertainty.

To evaluate the uncertainty from this source we recompute the antineutrino cross section with wrong-sign events in the RHC mode reweighted by the extracted neutrino low-ν flux. The difference is taken as the wrong-sign contamination uncertainty, which is less than 0.5% (0.2%) for the extracted antineutrino cross section (flux).

The overall 3.6% normalization uncertainty arises from the precision of the NOMAD data set in the energy range 12–22 GeV. We have assumed NOMAD data points in this region to have 100% correlated point-to-point systematic uncertainties in computing the weighted average error from their data. For antineutrinos and R_{CC} we assess an additional contribution to the uncertainty from the correction term, $G(\nu_0)$, by varying the GENIE-Hybrid cross section model parameters within their uncertainties prescribed by GENIE. The resulting uncertainty is negligible (less than 0.5% for all energies).

An error summary for the fluxes is shown in Fig. 5. The dominant systematic uncertainties on the shape for both the neutrino and antineutrino fluxes arise from limited
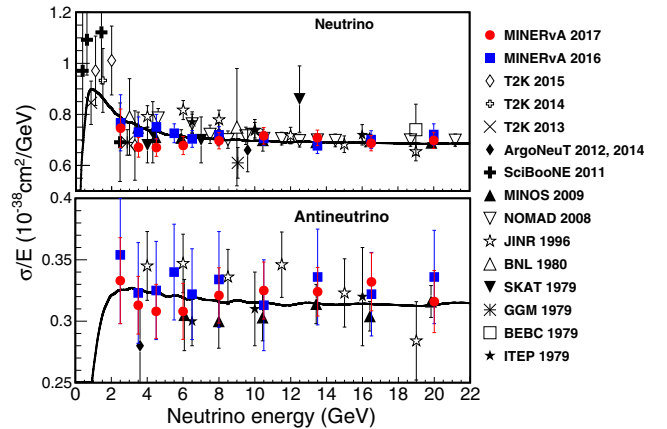

FIG. 10.   MINERvA measured neutrino and antineutrino charged-current inclusive cross sections (red circles and previous result from Ref. [4] shown with blue squares) compared with other measurements for neutrinos [6,7,27,34–46] (upper plot) and antineutrinos [6,40,47,48] (lower plot) on various nuclei in the same energy range. The reference curve shows the prediction of GENIE 2.8.4.
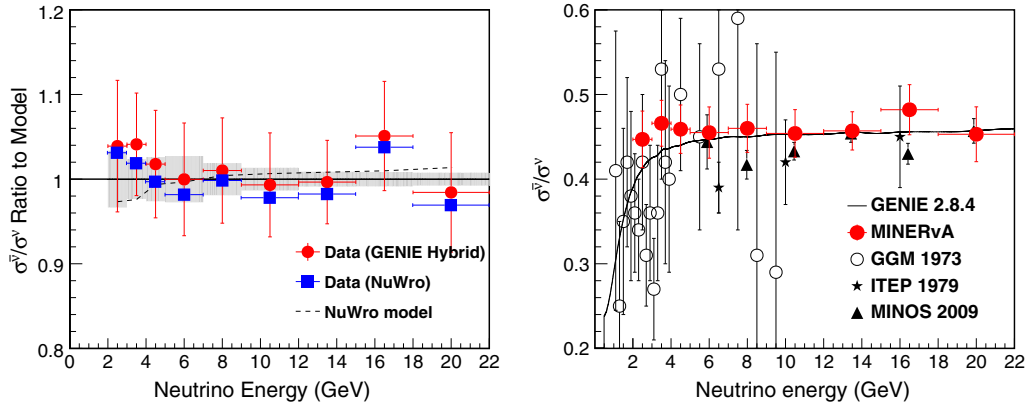
FIG. 11.   (Left) Ratio of measured R_{CC} to GENIE-Hybrid. Points are MINERvA data with default GENIE-Hybrid (circles) and alternative NuWro model (squares) used to compute model-based correction terms. GENIE-Hybrid data points are plotted with total error (sys.+stat). The dashed line shows the NuWro model. The shaded band shows the size of the cross section model systematic uncertainty. (Right) Comparison of MINERvA R_{CC} (corrected to an isoscalar target) with world measurements ([7,40] and [6]).

knowledge of muon and hadron energy scales. This uncertainty peaks at low energies and has a nontrivial energy dependence that is due to the combined effects from subcomponents having different precisions, as well as to the flux shape itself. The FSI uncertainty gives an effect that is also important, 3.5%, and nearly constant with energy. For antineutrinos, the statistical precision is poorer and is comparable to the systematic precision over most of the energy range. The statistical error in the data-based cross normalization factor $\alpha(\nu_0)$ (Table II), dominates the statistical precision below 12 GeV and is responsible for the detailed shape features in the uncertainty band.[2]

Neutrino and antineutrino cross section uncertainty components are summarized in Fig. 6. Many systematic effects cause changes that are similar in the cross section and flux samples and partially cancel in the measured cross section. The dominant uncertainty is from the cross section model at low energy, while normalization dominates at high energies. Neutrino and antineutrino cross sections have comparable systematic errors but the statistical precision is poorer for antineutrinos, and it dominates the error in all but the lowest energy bin.

The uncertainties on the cross section ratio, R_{CC}, are summarized in Fig. 7. Energy scale uncertainties nearly cancel in this ratio, and the sizes of effects from FSI and many model uncertainties are reduced. The dominant remaining uncertainties are from the M_A^{RES} cross section model parameter and the effect of implementing the RPA model in GENIE 2.8.4. The corresponding cross section components produce sizable shape effects on the visible energy in the low-ν region. Different final states in neutrino versus antineutrino interactions reduce cancellation effects in these components for the ratio. The overall uncertainty in

R_{CC} is dominated by statistical uncertainty in the antineutrino sample.

VIII. FLUX AND CROSS SECTION RESULTS

The extracted low-ν flux (Table IV) is shown in Fig. 8 where it is compared to the MINERvA simulated flux of Ref. [17]. The latter flux is constrained using hadron production data and a detailed GEANT4 [29] beam line simulation. The extracted flux low-ν is in reasonable agreement with the simulation for both modes.[3] The low-ν measurement prefers a smaller neutrino flux below 7 GeV (approximately 5%) while a larger flux is preferred for both neutrinos and antineutrinos (2%–12% for neutrinos, up to 16% for antineutrinos) in the >7 GeV range. The low-ν flux compared to the flux of the tuned production-based simulation achieves better precision for neutrinos (by 30% for E_ν above 3 GeV) and comparable for antineutrinos.

The measured cross sections (Table IV) are shown in Fig. 9 compared with the GENIE-Hybrid model. The data (red points), extracted using GENIE-Hybrid for model corrections, favor a lower total cross section in the region 2–9 GeV, where data lie below the curves (by up to ~2σ) for neutrinos. Antineutrino data also favor a lower cross section in the same region, but agree with models within the precision of the data, which have larger statistical uncertainties. For comparison, we also extract results using Eqs. (10) and (11) and NuWro (squares) to compute explicit model correction terms.[4] We omit error bars from

---

[2]Features occur where the ν_0 cut value changes at 3, 7, and 12 GeV.

[3]Our previous measurement uses an earlier version of the simulated flux as described in [4].

[4]GENIE 2.8.4 with FSI turned on is used to simulate the fully reconstructed MINERvA samples, and to correct for detector effects we deliberately turn the FSI processes off in NuWro, to avoid double counting them.

NuWro-based points, which use the same raw binned data, and therefore have the same (correlated) statistical and detector-related systematic uncertainties. The shaded band shows the size of the estimated model systematic uncertainty (computed from the GENIE-Hybrid model) which spans the differences between the extracted cross section values. The NuWro model has a different treatment of the low-ν region than GENIE, including a different axial mass parameter ($M_A = 1.2$ GeV), a transverse enhancement model (TEM) [32]) to account for the meson exchange current (MEC) scattering contribution, and a duality-based treatment in the resonance region [33]. The two sets of extracted cross sections show significant differences at low energies that reflect different modeling of the kinematic acceptance correction (A_{CC}^{KIN}), which is large for $E_\nu < 7$ GeV. QE and MEC components, which dominate the lowest energy bin, have a harder muon spectrum resulting in better acceptance in the NuWro model. GENIE kinematic acceptance is better in the 3–7 GeV energy range for the resonance and deep inelastic scattering (DIS) components, which become dominant above 3 GeV. At high energies, the normalization method removes the effect of correction differences between the two models for the neutrino data points. For antineutrinos, the GENIE-Hybrid results are systematically above those for the NuWro model by a few percent at high energies. We have applied the GENIE-Hybrid quark mixing correction $G(\nu_0)$ to the NuWro data points (NuWro does not include quark mixing by default). Figure 10 shows a comparison of the measured charged-current total cross sections with world neutrino data [6,7,27,34–46]. We apply a nonisoscalarity correction[5] to other data sets to compare with our isoscalar-corrected carbon measurement. The neutrino cross section is in good agreement with other measurements that overlap in this energy range and is among the most precise in the resonance-dominated region (2–7 GeV). Comparisons with world antineutrino data [6,40,47,48] are also shown. Our data add information in the region below 10 GeV where previous antineutrino data are sparse and improve precision and coverage, especially in the region below 6 GeV. Our results are in agreement with precise data on other nuclei [6] in the neutrino energy region of overlap (>6 GeV) and provide the most precise measurement of the antineutrino cross section below 5 GeV to date.

The measured cross section ratio, R_{CC}, is shown in Fig. 11 compared with GENIE and NuWro models and with world data [6,7,40]. Measured points are extracted using GENIE-Hybrid (circles) and NuWro (squares) for model corrections. The measured R_{CC} lies above the model

[5]Corrections for SciBooNE CH target points with energies in the range 0.38–2.47 GeV are 1.085, 1.06, 1.038, 1.033, 1.028, 1.028, respectively. We correct T2K 2013 (CH target at $E = 0.85$ GeV) by 1.04, T2K 2014 (iron at $E = 1.5$ GeV) by 0.977, T2K 2015 (iron at $E = 1$ GeV, 2 GeV, and 3 GeV) by 0.971, 0.976 and 0.977, respectively.

TABLE IV. Summary of measured quantities. Neutrino flux $\Phi^\nu(E)$ and antineutrino flux $\Phi^{\bar\nu}(E)$ and their errors (columns 1 and 3) are in units of neutrinos/m²/GeV/10⁶ pot. Neutrino cross section $\sigma^\nu(E)/E$ and antineutrino cross section $\sigma^{\bar\nu}(E)/E$ and their errors (columns 2 and 4) are in units of 10⁻³⁸ cm²/GeV. Columns labeled σ_{stat}, σ_{sys}, and σ_{tot} give the statistical (stat), systematic (sys), and total (tot) errors, respectively.

E GeV	$\Phi^\nu(E)$ neutrinos/m²/GeV/10⁶ POT				$\sigma^\nu(E)/E$ 10⁻³⁸ cm²/GeV				$\Phi^{\bar\nu}(E)$ neutrinos/m²/GeV/10⁶ POT				$\sigma^{\bar\nu}(E)/E$ 10⁻³⁸ cm²/GeV				R_{CC}			
	Φ^ν	σ_{stat}	σ_{sys}	σ_{tot}	σ^ν/E	σ_{stat}	σ_{sys}	σ_{tot}	$\Phi^{\bar\nu}$	σ_{stat}	σ_{sys}	σ_{tot}	$\sigma^{\bar\nu}/E$	σ_{stat}	σ_{sys}	σ_{tot}	R_{CC}	σ_{stat}	σ_{sys}	σ_{tot}
2.5	70.290	1.837	6.446	6.702	0.746	0.020	0.072	0.075	68.851	4.589	6.155	7.678	0.333	0.023	0.026	0.035	0.447	0.029	0.017	0.033
3.5	78.716	1.508	4.534	4.778	0.671	0.013	0.036	0.038	66.833	3.562	3.743	5.167	0.313	0.017	0.016	0.024	0.466	0.024	0.012	0.027
4.5	30.052	0.624	1.842	1.945	0.670	0.015	0.031	0.034	24.171	1.348	1.472	1.996	0.308	0.018	0.013	0.022	0.459	0.026	0.013	0.029
6.0	9.557	0.212	0.550	0.590	0.678	0.016	0.032	0.036	6.676	0.392	0.385	0.550	0.308	0.019	0.013	0.023	0.455	0.027	0.014	0.030
8.0	5.269	0.103	0.258	0.278	0.697	0.015	0.029	0.032	3.017	0.160	0.143	0.214	0.321	0.018	0.013	0.022	0.460	0.027	0.010	0.028
10.5	3.136	0.064	0.158	0.170	0.716	0.015	0.029	0.033	1.625	0.090	0.080	0.120	0.325	0.019	0.013	0.023	0.454	0.027	0.007	0.028
13.5	1.916	0.034	0.099	0.104	0.708	0.014	0.027	0.031	0.895	0.035	0.044	0.056	0.324	0.015	0.013	0.020	0.457	0.022	0.007	0.023
16.5	1.173	0.024	0.059	0.063	0.687	0.015	0.026	0.030	0.437	0.022	0.025	0.033	0.331	0.020	0.013	0.024	0.482	0.029	0.007	0.030
20.0	0.651	0.014	0.034	0.037	0.698	0.017	0.027	0.032	0.229	0.014	0.014	0.019	0.316	0.022	0.013	0.025	0.453	0.032	0.006	0.032

predictions at low energies and favors a flatter extrapolation into that region than do the models, which fall off below 5 GeV. The NuWro results are systematically below the GENIE-Hybrid results by a few percent, tracking the differences seen in the antineutrino cross section level in the numerator (discussed above). The differences between GENIE-Hybrid-based and NuWro-based R_{CC} measurements at lower energies are less significant than differences seen in the cross sections from the two models. The shaded band, which spans the NuWro versus GENIE-Hybrid point differences, shows the size of the estimated systematic uncertainty from model sources. Our result is in good agreement with the recent measurement from MINOS on an iron target in the region where they overlap ($E_\nu > 6$ GeV). This measurement is the only precise determination of R_{CC} in the $E_\nu < 6$ GeV region. It spans neutrino energies from 2 to 22 GeV, a range which is highly relevant to ongoing and future oscillation experiments.

IX. CONCLUSION

We present the first precise measurement of the ratio of antineutrino to neutrino cross sections, R_{CC}, in the region below 6 GeV, which is important for future long baseline neutrino oscillation experiments. Our measurement, with precision in the range of 5.0%–7.5%, represents an improvement by nearly a factor of 4 over the previous measurements in this region [7]. We measure neutrino and antineutrino cross sections that extend the reach for antineutrino data to low energies and are among the most precise in the few GeV energy range. Two leading neutrino generators, GENIE and NuWro, both overestimate the measured inclusive CC cross sections at the level of 4%–10% as energy decreases from 9 GeV to 2 GeV. We also present measured total and low-ν fiducial rates that can be used to obtain the cross sections and their ratio with other models. In the near future, this will allow our data to be used with new models that will have improved treatments of nuclear effects and low energy scattering processes.

The cross section ratio R_{CC} is found to have systematic uncertainties that are significantly smaller than those associated with either of the CC inclusive cross sections, due to the cancellation of common systematic uncertainties. We demonstrate the robustness of R_{CC} by comparing results using two different models (GENIE-Hybrid and NuWro). The differences are found to be smaller than in the individual cross section measurements and are comparable with the size of estimated model systematic uncertainties.

[1] R. Acciarri *et al.* (DUNE Collaboration), arXiv:1512.06148.

[2] K. Abe *et al.* (Hyper-Kamiokande Proto-Collaboration), Prog. Theor. Exp. Phys. **2015**, 53C02 (2015).

[3] W. Marciano and Z. Parsa, Nucl. Phys. B, Proc. Suppl. **221**, 166 (2011).

[4] J. Devan *et al.* (MINERvA Collaboration), Phys. Rev. D **94**, 112007 (2016).

[5] K. A. Olive *et al.* (Particle Data Group Collaboration), Chin. Phys. C **38**, 090001 (2014).

[6] P. Adamson *et al.* (MINOS Collaboration), Phys. Rev. D **81**, 072002 (2010).

[7] T. Eichten *et al.*, Phys. Lett. B **46B**, 274 (1973).

[8] A. Gazizov and M. P. Kowalski, Comput. Phys. Commun. **172**, 203 (2005).

[9] C. Andreopoulos *et al.*, Nucl. Instrum. Methods Phys. Res., Sect. A **614**, 87 (2010).

[10] O. Buss, T. Gaitanos, K. Gallmeister, H. van Hees, M. Kaskulov, O. Lalakulich, A. B. Larionov, T. Leitner, J. Weil, and U. Mosel, Phys. Rep. **512**, 1 (2012).

[11] D. Autiero, Nucl. Phys. B, Proc. Suppl. **139**, 253 (2005).

[12] D. Casper, Nucl. Phys. B, Proc. Suppl. **112**, 161 (2002).

[13] G. Battistoni, P. R. Sala, M. Lantz, A. Ferrari, and G. Smirnov, Acta Phys. Pol. B **40**, 2491 (2009).

[14] T. Golan, C. Juszczak, and J. T. Sobczyk, Phys. Rev. C **86**, 015505 (2012).

[15] P. A. Rodrigues *et al.* (MINERvA Collaboration), Phys. Rev. Lett. **116**, 071802 (2016).

[16] P. Adamson *et al.*, Nucl. Instrum. Methods Phys. Res., Sect. A **806**, 279 (2016).

[17] L. Aliaga *et al.* (MINERvA Collaboration), Phys. Rev. D **94**, 092005 (2016).

[18] L. Aliaga *et al.* (MINERvA Collaboration), Nucl. Instrum. Methods Phys. Res., Sect. A **743**, 130 (2014).

[19] D. G. Michael *et al.* (MINOS Collaboration), Nucl. Instrum. Methods Phys. Res., Sect. A **596**, 190 (2008).

[20] C. Andreopoulos *et al.*, Nucl. Instrum. Methods Phys. Res., Sect. A **614**, 87 (2010).

[21] C. Andreopoulos, C. Barry, S. Dytman, H. Gallagher, T. Golan, R. Hatcher, G. Perdue, and J. Yarba, arXiv:1510.05494.

[22] J. Nieves, J. E. Amaro, and M. Valverde, Phys. Rev. C **70**, 055503 (2004); **72**, 019902(E) (2005).

[23] J. Nieves, I. Ruiz Simo, and M. J. Vicente Vacas, Phys. Rev. C **83**, 045501 (2011).

[24] P. Rodrigues, C. Wilkinson, and K. McFarland, Eur. Phys. J. C **76**, 474 (2016).

[25] S. R. Mishra, in *Proceedings of the Workshop on Hadron Structure Functions and Parton Distributions*, edited by D. Geesaman *et al.* (World Scientific, Batavia, IL, 1990), p. 84.

[26] W. Seligman, Ph.D. thesis, Columbia University, 1997, Nevis 292.

[27] Q. Wu *et al.* (NOMAD Collaboration), Phys. Lett. B **660**, 19 (2008).

[28] L. Aliaga *et al.* (MINERvA Collaboration), Nucl. Instrum. Methods Phys. Res., Sect. A **789**, 28 (2015).

[29] S. Agostinelli *et al.* (GEANT4 Collaboration), Nucl. Instrum. Methods Phys. Res., Sect. A **506**, 250 (2003).

[30] L. Ren, Ph.D. thesis, University of Pittsburgh, 2017.

[31] P. A. Rodrigues *et al.* (MINERvA Collaboration) (to be published).

[32] A. Bodek, H. S. Budd, and M. E. Christy, Eur. Phys. J. C **71**, 1726 (2011).

[33] K. M. Graczyk, C. Juszczak, and J. T. Sobczyk, Nucl. Phys. A**781**, 227 (2007).

[34] S. J. Barish *et al.*, Phys. Lett. **66B**, 291 (1977).

[35] S. J. Barish *et al.*, Phys. Rev. D **19**, 2521 (1979).

[36] C. Baltay *et al.*, Phys. Rev. Lett. **44**, 916 (1980).

[37] N. J. Baker, P. L. Connolly, S. A. Kahn, M. J. Murtagh, R. B. Palmer, N. P. Samios, and M. Tanaka, Phys. Rev. D **25**, 617 (1982).

[38] S. Ciampolillo *et al.* (Aachen-Brussels-CERN-Ecole Poly-Orsay-Padua, Gargamelle Neutrino Propane), Phys. Lett. **84B**, 281 (1979).

[39] D. S. Baranov *et al.*, Phys. Lett. **81B**, 255 (1979).

[40] A. I. Mukhin, V. F. Perelygin, K. E. Shestermanov, A. A. Volkov, A. S. Vovenko, and V. P. Zhigunov, Yad. Fiz. **30**, 1014 (1979) [Sov. J. Nucl. Phys. **30**, 528 (1979)].

[41] V. B. Anikeev *et al.*, Z. Phys. C **70**, 39 (1996).

[42] Y. Nakajima *et al.* (SciBooNE Collaboration), Phys. Rev. D **83**, 012005 (2011).

[43] C. Anderson *et al.* (ArgoNeuT Collaboration), Phys. Rev. Lett. **108**, 161802 (2012).

[44] K. Abe *et al.* (T2K Collaboration), Phys. Rev. D **87**, 092003 (2013).

[45] K. Abe *et al.* (T2K Collaboration), Phys. Rev. D **93**, 072002 (2016).

[46] R. Acciarri *et al.* (ArgoNeuT Collaboration), Phys. Rev. D **89**, 112003 (2014).

[47] A. E. Asratian *et al.*, Phys. Lett. **76B**, 239 (1978).

[48] G. Fanourakis, L. K. Resvanis, G. Grammatikakis, P. Tsilimigras, A. Vayaki, U. Camerini, W. F. Fry, R. J. Loveless, J. H. Mapp, and D. D. Reeder, Phys. Rev. D **21**, 562 (1980).